Space Weather

RESEARCH ARTICLE
10.1002/2017SW001776

Special Section:
Space Weather Events of 4–10 September 2017

Midlatitude Plasma Bubbles Over China and Adjacent Areas During a Magnetic Storm on 8 September 2017

Ercha Aa[1,2], Wengeng Huang[1], Siqing Liu[1,3], Aaron Ridley[2], Shasha Zou[2], Liqin Shi[1,3], Yanhong Chen[1], Hua Shen[1], Tianjiao Yuan[1], Jianyong Li[4], and Tan Wang[4]

[1]National Space Science Center, Chinese Academy of Sciences, Beijing, China, [2]Department of Climate and Space Sciences and Engineering, University of Michigan, Ann Arbor, MI, USA, [3]College of Earth and Planetary Science, University of Chinese Academy of Sciences, Beijing, China, [4]National Earthquake Infrastructure Service, Beijing, China

Key Points:
- Postsunset midlatitude plasma bubbles were observed over China and adjacent areas using GNSS TEC, Swarm Ne, and ionosonde data
- The plasma bubbles were triggered by PPEF and TID in equatorial regions and extended along the magnetic field lines to 50°N (45.5 MLAT)
- Plasma bubbles might reach an altitude of 6,600 km over the magnetic equator with the upper limit of upward drift speed being around 700 m/s

Correspondence to:
E. Aa,
aercha@nssc.ac.cn

Citation:
Aa, E., Huang, W., Liu, S., Ridley, A., Zou, S., Shi, L., et al. (2018). Midlatitude plasma bubbles over China and adjacent areas during a magnetic storm on 8 September 2017. *Space Weather*, *16*, 321–331. https://doi.org/10.1002/2017SW001776

Received 19 NOV 2017
Accepted 5 MAR 2018
Accepted article online 9 MAR 2018
Published online 30 MAR 2018

Abstract This paper presents observations of postsunset super plasma bubbles over China and adjacent areas during the second main phase of a storm on 8 September 2017. The signatures of the plasma bubbles can be seen or deduced from (1) deep field-aligned total electron content depletions embedded in regional ionospheric maps derived from dense Global Navigation Satellite System networks, (2) significant equatorial and midlatitudinal plasma bite-outs in electron density measurements on board Swarm satellites, and (3) enhancements of ionosonde virtual height and scintillation in local evening associated with strong southward interplanetary magnetic field. The bubbles/depletions covered a broad area mainly within 20°–45°N and 80°–110°E with bifurcated structures and persisted for nearly 5 hr (~13–18 UT). One prominent feature is that the bubbles extended remarkably along the magnetic field lines in the form of depleted flux tubes, reaching up to midlatitude of around 50°N (magnetic latitude: 45.5°N) that maps to an altitude of 6,600 km over the magnetic equator. The maximum upward drift speed of the bubbles over the magnetic equator was about 700 m/s and gradually decreased with altitude and time. The possible triggering mechanism of the plasma bubbles was estimated to be storm time eastward prompt penetration electric field, while the traveling ionospheric disturbance could play a role in facilitating the latitudinal extension of the depletions.

1. Introduction

Plasma bubbles refer to irregular structures of plasma density depletion, which are typical characteristics of nighttime ionosphere over equatorial and low-latitude regions. Plasma bubbles with different scale sizes can manifest themselves as spread-F echoes on ionograms (Abdu et al., 2003), plume-like structures in radar backscatter maps (Woodman & La Hoz, 1976), airglow density depletions in all-sky images (Kelley et al., 2002), and very high frequency/ultrahigh frequency scintillations of satellites signals (Basu et al., 2005; Bhattacharyya et al., 2001). It is widely considered that the plasma bubbles are generated by the Rayleigh-Taylor (R-T) instability in the bottomside ionosphere after sunset and evolve nonlinearly penetrating the F peak to the topside ionosphere (Fejer et al., 1999; Kelley et al., 1976; Ma & Maruyama, 2006; Ott, 1978). They sometimes form into wedge-like structures extended along the magnetic field lines (Tsunoda, 1980; Tsunoda et al., 1982). Although various mechanisms (such as electric field, neutral wind, and gravity waves) can play a role in triggering R-T instability, the most efficient seeding factor of plasma bubbles over equatorial/low-latitude regions is the zonal electric field (e.g., Abdu et al., 1997; Fejer et al., 1999; Kil, 2015; Li, Ning, Zhao, et al., 2009). The postsunset enhancement of eastward electric field, also known as prereversal enhancement (PRE), is responsible for the enhanced equatorial upward drift that causes density perturbations to grow by the R-T instability mechanism, which may lead to the formation of plasma bubbles (Abadi et al., 2015; Abdu, 2012; Farley et al., 1986; Retterer & Roddy, 2014).

During geomagnetic storms, the development of plasma bubbles can be enhanced or suppressed depending primarily on two types of perturbation electric fields: (1) the prompt penetration electric field (PPEF) created by solar wind-magnetosphere dynamo associated with southward turning of interplanetary magnetic field (IMF) B_z; (2) ionospheric disturbance dynamo electric field (DDEF) induced by changes in global thermospheric circulation due to auroral Joule heating, which may lead to the inhibition of postsunset plasma

bubbles occurrence (Carter et al., 2016; Li, Ning, Liu, et al., 2009, Ramsingh et al., 2015; Scherliess & Fejer, 1997). The PPEF can be superposed on the normal dusk PRE to cause larger ionospheric uplift and thus facilitate the development of plasma bubbles (Abdu et al., 2003; Basu et al., 2001, 2007; Huang et al., 2010; Tulasi Ram et al., 2008). The storm effect of these two competing mechanisms on plasma bubbles is an important concern in ionosphere research community.

The occurrence of plasma bubbles and associated signatures of irregularities can even be observed at middle latitude, which could be caused either by an extension of equatorial plasma bubbles along the magnetic field lines after rising to a relatively high altitude or by local Perkins instability (Perkins, 1973). Recently, several studies have indicated that the equatorial plasma irregularities can reach high altitudes and extend to higher latitudes in the form of depleted flux tubes. For example, it was reported by Kelley et al. (2003) and Makela and Kelley (2003) that the equatorial plasma depletions can be viewed in all-sky airglow images at Maui, Hawaii (magnetic latitude [MLAT]: 21.3°N). Mendillo et al. (2005, 2018) conducted simultaneous observation by using radar measurements and all-sky images at Arecibo observatory (MLAT: 30°N), and the study showed the field-aligned structures in the images corresponding to the flux tubes of plasma density depletions. Ma and Maruyama (2006) reported a case in which a super plasma bubble could be detected at MLAT 31°N by using dense GPS network observations. Foster and Rich (1998) reported that the plasma depletions can be measured at MLAT 35°–37°N by using Millstone Hill incoherent scatter radar and the DMSP satellites. Katamzi-Joseph et al. (2017) found that the plasma bubbles can extend as far north as ~42°N (MLAT: ~39°N) using Global Navigation Satellite System (GNSS) TEC and ion measurements from DMSP satellites. Cherniak and Zakharenkova (2016) reported super plasma bubbles in Europe for more than 8 hr reaching ~40°–45°N (MLAT: ~35°–41°N), based on GNSS TEC as well as measurements from Swarm and DMSP satellites. Huang et al. (2007) reported that during intense storms, depleted flux tubes associated with large-scale plasma bubbles can extend to much higher latitudes (MLAT: ~46°N).

In this paper, we present unique observations of super plasma bubbles at MLAT~15°–45°N over China and adjacent areas during an intense storm on 8 September 2017. It was found that the storm time PPEF contributed to the generation and migration of the super plasma bubbles, which were detected and recorded by using observations from ionosonde, dense GNSS network, and the Swarm satellites. Moreover, traveling ionospheric disturbance (TID) could also played a role in facilitating the latitudinal extension of the bubbles.

2. Data Description

Measurements from multiple instruments were analyzed to study the characteristics of plasma bubbles under the influence of the geomagnetic storm on 8 September 2017. The solar wind and geomagnetic conditions during the storm are described in Figure 1 by using solar wind speed, IMF B_z component, interplanetary electric field (IEF) E_y component, the longitudinal asymmetric index (ASY-H) that represents the auroral activity, and the symmetric index (SYM-H) as the high-resolution *Dst* index.

The most important information about plasma bubbles are provided by the TEC data from ground-based GNSS measurements. The GNSS data come from Crustal Movement Observation Network of China (CMONOC) and the International GNSS Service (IGS). CMONOC consists of 260 GNSS receivers covering China mainland, and there are 38 stations of IGS located within China and adjacent regions. For more details on the distribution of GNSS stations and the procedures of TEC derivation, readers may refer to Aa et al. (2015).

Besides TEC data, the ionosonde measurements from Sanya (18.3°N, 109.4°E) and GNSS scintillation measurements from Kunming (24.2°N, 103.4°E) and Guangzhou (23.2°N, 113.3°E), as well as the in situ electron density measurements on board the Swarm A and Swarm C satellites at an orbit at altitude around 450 km, are used to analyze the signature of plasma bubbles.

3. Observational Results

During the time periods of 7–8 September 2017, two coronal mass ejections (CMEs) passed Earth successively and generated an intense geomagnetic storm with a double main phase. Figures 1a–1e show the temporal variation of the solar wind speed, IMF B_z component, IEF E_y component, SYM-H index, and the ASY-H index for the above mentioned periods. Figures 1a and 1b show that the IMF B_z turned southward at around 20:40 UT on 7 September and remained negative at nearly constant level for 2 hr then suddenly decreased to a minimum value of −31.2 nT at 23:31 UT on 7 September, along with a sharp increase of the solar wind speed due

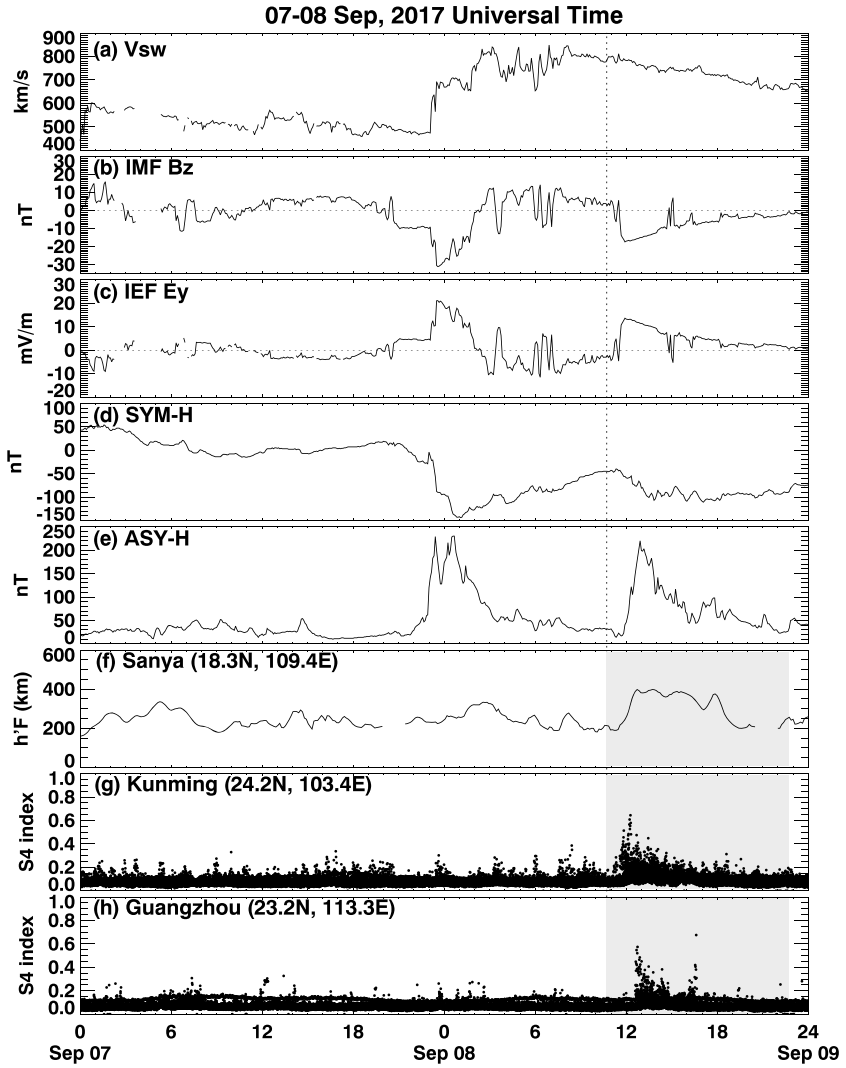

Figure 1. Time series of (a) solar wind speed, (b) interplanetary magnetic field (IMF) B_z, (c) interplanetary electric field (IEF) E_y, (d) SYM-H index, (e) ASY-H index, (f) ionospheric virtual height (h'F) over Sanya, and S4 scintillation index during the period of 7–8 September 2017 for Kunming (g) and Guangzhou (h). The solar wind and IMF data have been shifted to the nose of the Earth's bow shock. The shaded areas represent the local dusk to dawn period at these stations.

to the compression and interaction of these two CMEs. Figure 1d illustrates that the minimum value of SYM-H for the first storm main phase reached −144 nT at 01:05 UT on 8 September. During the recovery phase, the next CME reamplified the storm with a second main phase onset at 11:35 UT. The IMF B_z decreased to −17.4 nT at 11:55 UT on 8 September and remained negative for several hours. SYM-H dropped to a second minimum value of −111 nT at 17:05 UT on 8 September.

Figure 1f shows the corresponding variation of ionospheric virtual height (h'F) over a low-latitude station Sanya (18.3°N, 109.4°E, dip angle: 11.3°). The local dusk to dawn intervals of the station on 8 September are marked by shaded areas. Figure 1f shows that compared with the previous evening, the h'F of Sanya station exhibited a considerable postsunset increase at around 12:45 UT on 8 September, which was consistent with the pronounced increase (decrease) of IEF E_y (SYM-H). These near simultaneous enhancements of h'F and IEF E_y indicate that there was a prompt penetration of eastward electric field into middle- and low-latitude regions at local dusk hours on 8 September, which added onto the normal postsunset PRE of zonal electric field, caused larger upward plasma drifts, and generated conditions favorable for the formation of plasma bubbles. Figures 1g and 1h show the measurements of L-band amplitude scintillations index S4 from GPS/Beidou satellites in the adjacent stations: Kunming (24.2°N, 103.4°E, dip angle: 17.7°)

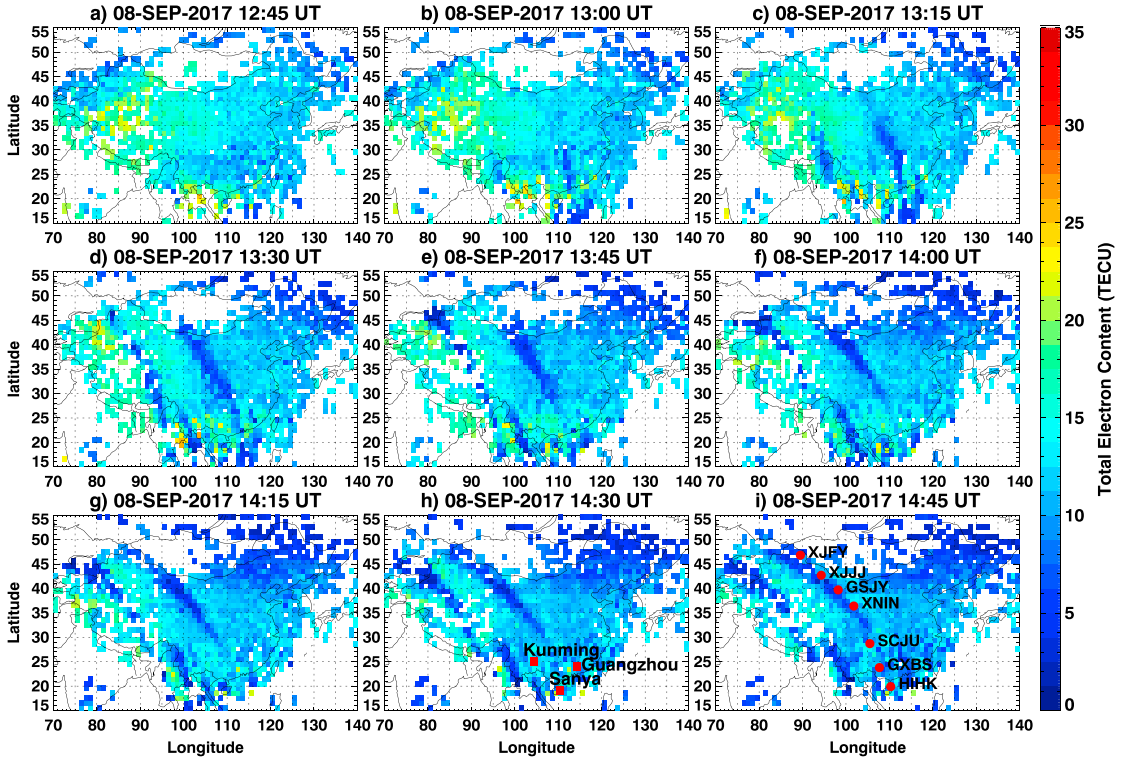

Figure 2. Gridded total electron content maps over China and adjacent areas with 15-min interval during 12:45–14:45 UT on 8 September 2017. The distribution of ionosonde/scintillation stations used in current study is shown in Figure 2h. Seven Global Navigation Satellite System stations are marked in Figure 2i to track the trace of irregularities.

and Guangzhou (23.2°N, 113.3°E, dip angle: 16.7°). Weak to moderate scintillations started from around 11:45–12:00 UT on 8 September, illustrating the possible generation of plasma irregularities/bubbles induced by the geomagnetic storm.

TEC data can be used to further confirm the existence of plasma bubbles. Figures 2 and 3 show a series of gridded vertical TEC maps over China and adjacent areas at 15-min intervals during 12:45–17:00 UT on 8 September 2017. An elevation cutoff of 30° was used to avoid multipaths effects. The resolution of the map is 1° × 1° and was generated by selecting the median of all available measurements in each bin as the estimated grid value, with no interpolation being applied. The signatures of the plasma bubbles appeared in the form of TEC depletions embedded in the maps mainly within 20°–45°N and 80°–110°E, which originated from the equatorial latitudes and then expanded northwestward approximately along the geomagnetic field lines. The depth of TEC depletions varied in the range of 5–15 TEC Unit (TECU, 10^{16} el/m^2). As shown in Figures 2b and 2c, two separate parallel structures of TEC depletion initiated around 13:00 UT, which could correspond to bifurcated branches of plasma bubbles as previously reported (e.g., Cherniak & Zakharenkova, 2016; Ma & Maruyama, 2006).

In order to further illustrate the characteristics of plasma bubbles, the rate of TEC index (ROTI; Pi et al., 1997) was derived by using dual frequency phase measurements of navigation signals, which can be used to represent the severity of GNSS phase fluctuations and to characterize the ionospheric irregularities. The time derivative of TEC (Rate of TEC change, ROT) was first calculated for all visible satellites with elevation angle greater than 30°. ROTI is defined as the 5-min standard deviation of ROT. For more details about ROTI, readers may refer to Pi et al. (1997) and Cherniak et al. (2014). Figures 4 and 5 present the ROTI maps with the same resolution and time interval as those of Figures 2 and 3. The irregularities were first seen in the low-latitude regions between 95°E and 120°E longitudinal sectors at 12:45 UT, which approximately corresponded to a local time between 19:00 and 20:45. The bubble-like structures bifurcated and further extended northwestward in the form of depleted flux tubes. The west branch reached ~45°N (MLAT: ~41°N) at 13:30 UT, indicating that the plasma bubbles could rise to an altitude of ~4,800 km over the magnetic equator. Similarly, the east branch migrated to a maximum latitude of ~50°N (MLAT: ~45.5°N) that corresponded to an altitude of ~6,600 km

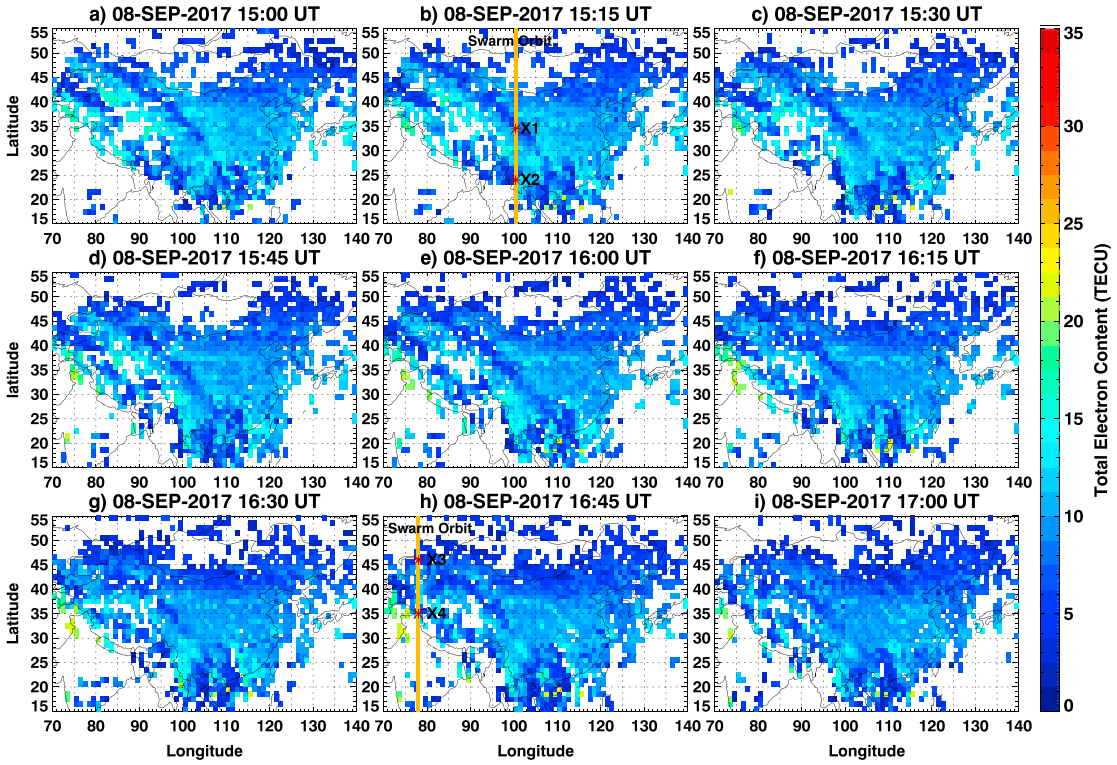

Figure 3. Same as Figure 2 but for time period of 15:00–17:00 UT on 8 September 2017. The Swarm satellite orbits are superimposed on total electron content depletions for Figures 3b and 3h with four points of intersection being marked by asterisks.

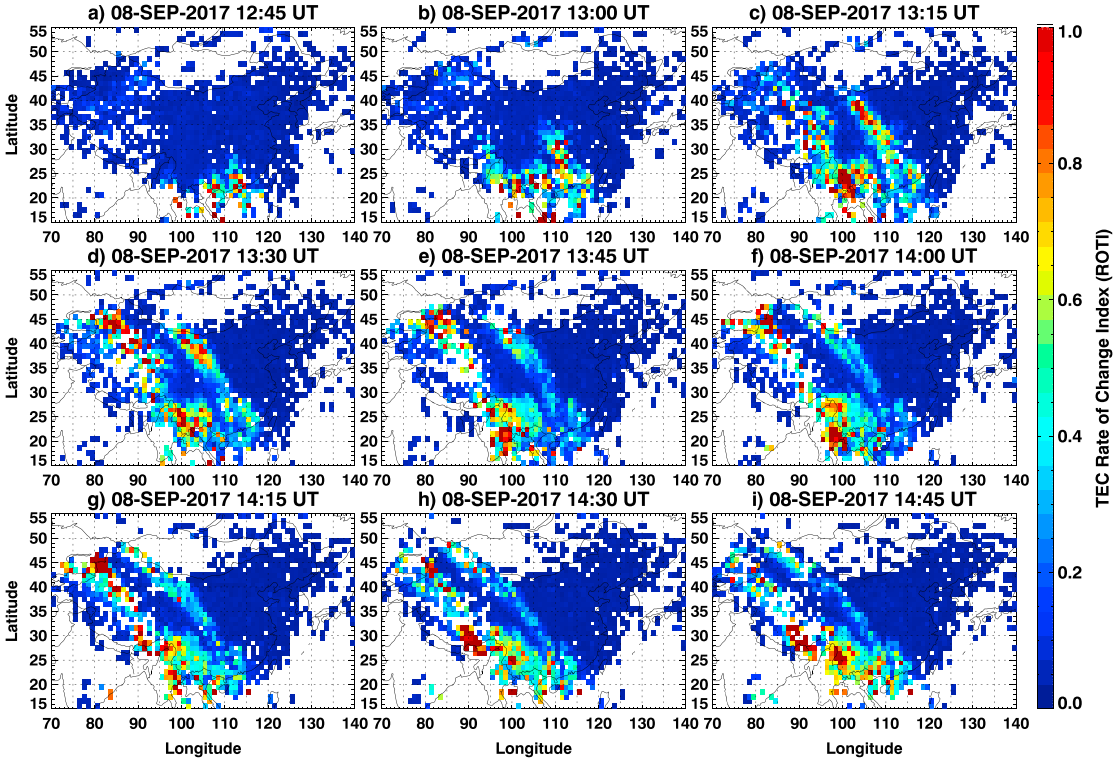

Figure 4. Rate of total electron content index (ROTI) maps of ionospheric irregularities over China and adjacent areas with 15-min interval during 12:45–14:45 UT on 8 September 2017.

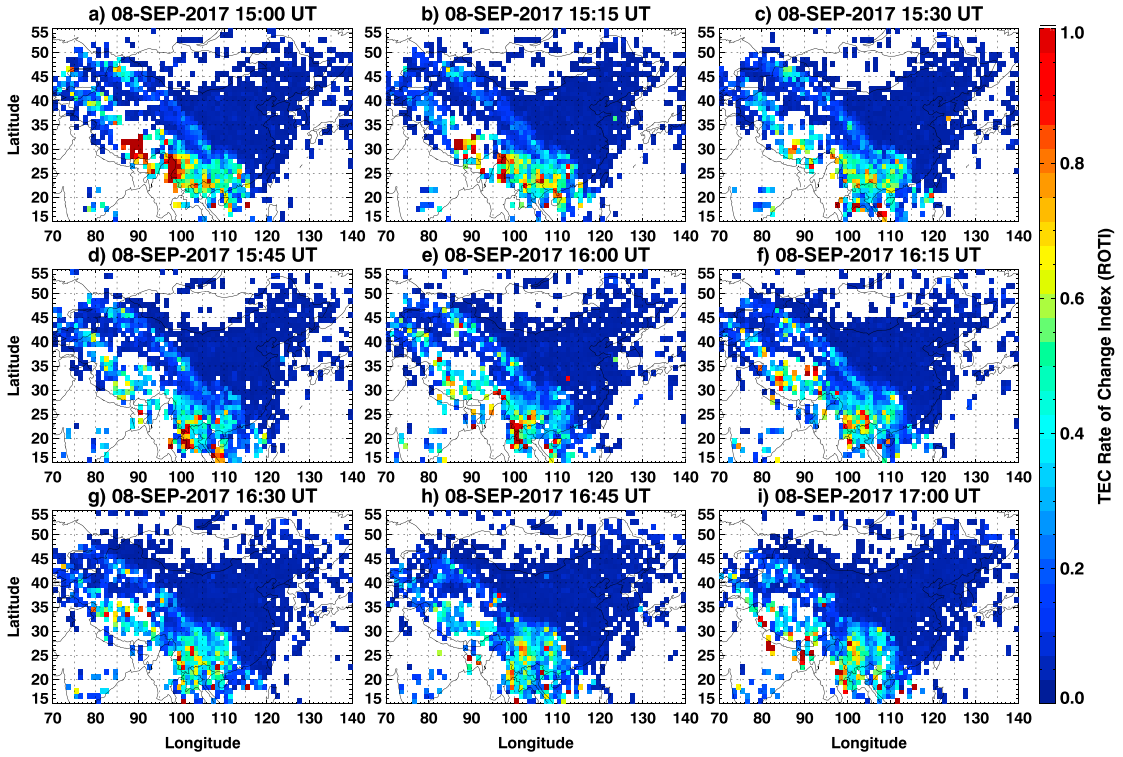

Figure 5. Same as Figure 4 but for time period of 15:00–17:00 UT on 8 September 2017.

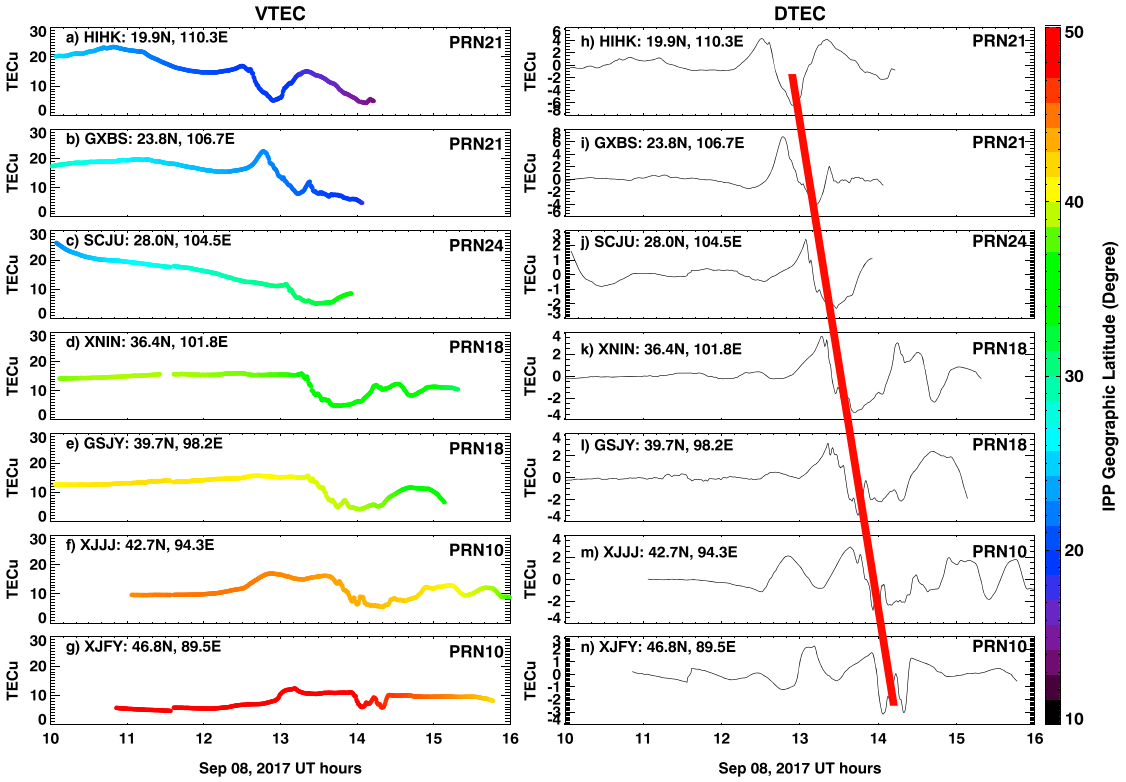

Figure 6. Temporal variation of total electron content (TEC) and detrended TEC over seven stations during 10–16 UT on 8 September 2017. The color bar shows the geographic latitude range of the ionospheric pierce points (IPP). The red thick line marks the propagation of the depletions.

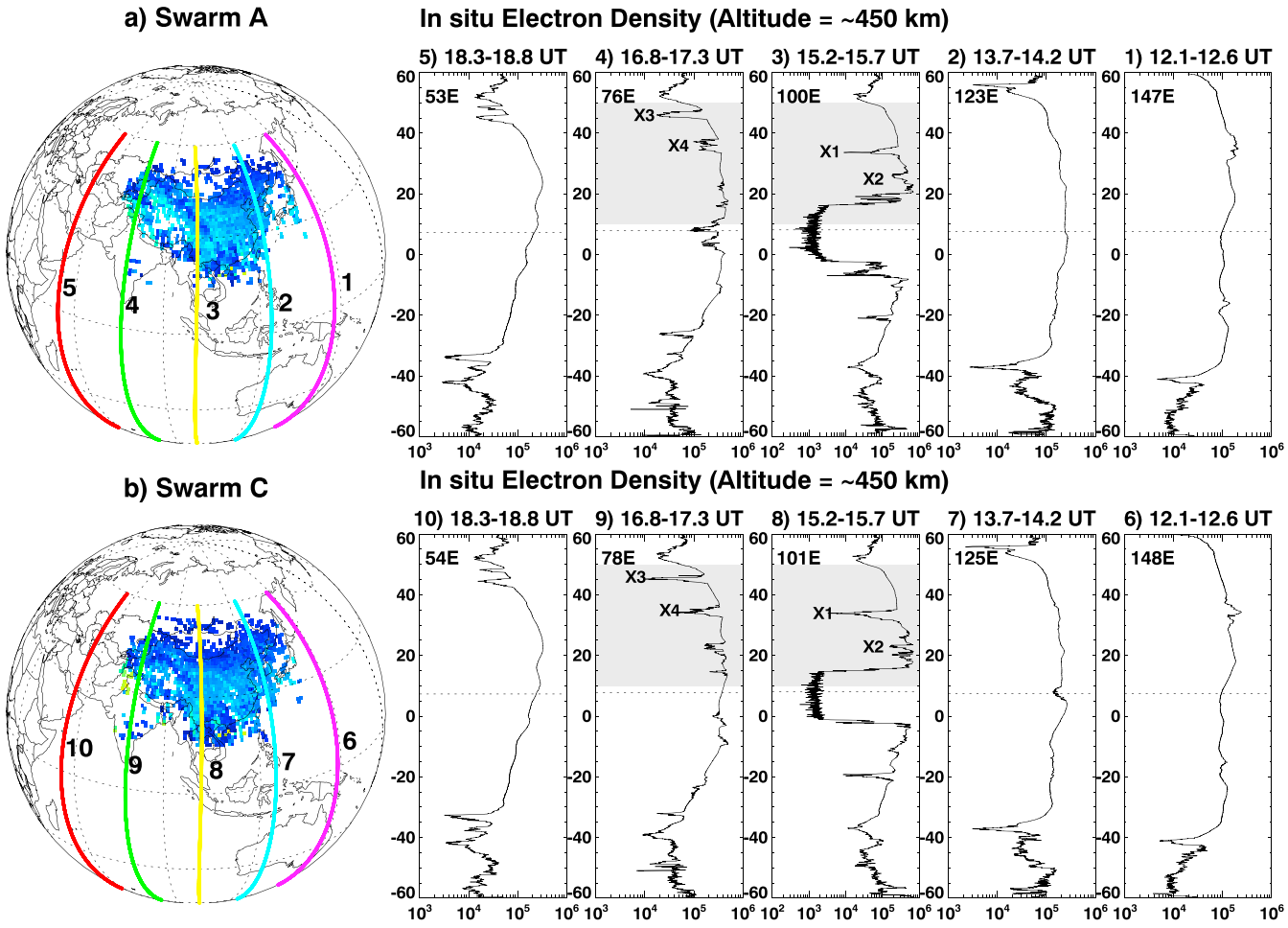

Figure 7. (a) (left) The global map with five different satellite orbit paths of Swarm A, with gridded total electron content at 15:15 UT being superimposed; (right) variation of in situ electron density as a function of geographic latitudes along these paths. (b) The same as Figure 7a but for Swarm C satellite with gridded total electron content at 16:45 UT being superimposed. The shaded areas represent plasma depletions over China and adjacent regions. Four intersection points X1–X4 that marked in Figures 3b and 3h are also shown here. The magnetic equator is indicated by dotted horizontal lines on the density-latitude profiles.

over the magnetic equator, similar to those indicated in Huang et al. (2007). TEC depletion and associated ROTI fluctuation continued for 5 hr and gradually subsided.

Figures 6a–6g show the temporal variation of ionospheric pierce points vertical TEC at seven stations between 10 and 16 UT on 8 September 2017 for PRNs 10, 18, 21, and 24. The locations of these stations are shown in Figure 2i, which were selected to be evenly distributed along the latitudinal extension of the irregularities as much as possible. The color bar represents the geographic latitudes of ionospheric pierce point, indicating that TEC depletions can be observed between 15°N and 50°N. Figures 6h–6n show the associated detrended TEC results to better illustrate the plasma depletion. The detrended TEC was calculated by subtracting the 1-hr moving average value of original TEC data. The inclined red thick line marks the trends of the negative wavefront. This can be used to calculate the horizontal phase speed of the depletion, which is estimated to be as much as ~800 m/s with roughly a northwestward direction. Considering the previous analysis of Figures 2 and 4, the rate of latitudinal extension of the depletion/irregularities traces in TEC and ROTI maps can be used to estimate the vertical drift speed of equatorial plasma bubbles. The scintillation started at around 1145 UT at Kunming station (MLAT: 17.7°), which corresponded to ~650-km altitude over magnetic equator; while the highest latitude reached by the TEC/ROTI at ~1315 UT is 45°N (MLAT: 40.5°), which corresponded to ~4,600-km altitude over magnetic equator. It can be estimated that the upward drift speed of plasma bubbles over the magnetic equator was ~700 m/s at around 13:15 UT and gradually decreased with increasing altitude and time.

Figure 7 shows satellite passes and the corresponding measurements of electron density from the Swarm constellation from 12 UT to 18 UT on 8 September 2017. Swarm A and Swarm C flew at an altitude of 440–460 km. They have nearby longitudes that approximately located in ~10 LT (ascending) and ~22 LT (descending) sectors. The geographic maps with different satellite orbit paths between 60°N and 60°S are shown in Figures 7a and 7b for Swarm A and Swarm C, respectively. The right panels show the variation of in situ electron density (Ne) with respect to latitude along these paths. Swarm B is not shown here since it did not pass over China and adjacent sectors in the local postsunset hours during this storm period. Swarm A measured no signatures of equatorial plasma bubbles in paths #1 (147°E) and #2 (123°E), though obvious plasma depletions were detected at ~40°S. However, the satellite in path #3 (100°E) measured a wide and drastic density depletion near the equator as low as 2×10^3 el/cm^2, which was 2–3 orders of magnitude lower than normal Ne conditions. The coverage of major depletion was between 10°S and 20°N with several minor negative spikes distributed in the middle latitudes of both hemispheres, which can be clearly distinguished from the main ionospheric midlatitude trough at around 50°–60°. Similar observations were made by Swarm C as shown in Figure 7b. The TEC results that coincide with path #3 (#8) at 15:15 UT and with path #4 (#9) at 16:45 UT are also superimposed on Figures 7a and 7b, respectively. Recall from Figures 3b and 3h that the same paths of Swarm were also shown there with four intersections between satellite paths and TEC depletions being marked. It can be seen that these intersections (X1–X4) correspond nicely to the midlatitude bite-outs in the plasma profiles. This demonstrates that the latitudinal elongated plasma depletion was mainly associated with plasma bubbles, though another factor that the Swarm orbit being below the F layer peak might also play a role in it. This bubble-associated extension of depletion was also reported by several studies (e.g., Basu et al., 2001; Cherniak & Zakharenkova, 2016; Huang et al., 2007; Kil et al., 2006). These studies indicate that the plasma bubbles can be lifted to higher altitudes with depletions being extended along the magnetic field lines to higher latitudes, as can be seen in paths #4 (#9) and #5 (#10). The equatorial Ne depletions along these paths were less obvious and gradually subsided, yet the signatures of plasma bubbles that had drifted to much higher latitudes can be detected at ~50°N and ~40°S. The shaded areas indicate deep plasma depletions over China and adjacent regions in accord with TEC depletions in Figures 2 and 3 as well as ROTI fluctuations in Figures 4 and 5.

4. Discussion

First, the results presented in the previous section indicate that there were significant equatorial plasma bubbles over China and adjacent sectors in local dusk hours on 8 September 2017, which were associated with strong PPEF as can be deduced from the simultaneously drastic change of IMF B_z, IEF, SYM-H, and ionosphere virtual height during the second main phase of the storm. It is generally assumed that PPEF is eastward (westward) during daytime through dusk sectors (midnight to dawn sectors) and can penetrate nearly instantly to low latitudes and has a relatively short duration (~1–2 hr); on the other hand, DDEF is westward (eastward) during daytime (nighttime), and the buildup time of the DDEF after storm onset is comparatively long (>3 hr) such that it may take up to 1–2 days before the equatorial ionospheric response can be fully observed (Fejer, 1991; Horvath & Lovell, 2013; Li, Ning, Liu, et al., 2009; Tulasi Ram et al., 2015). Huang (2008) and Huang et al. (2010) also pointed out that the PPEF is approximately proportional to the IEF during the storm main phase. Recall from Figures 1c and 1f that the IEF E_y drastically increased from −6.5 (11:35 UT) to 13.76 mV/m (11:58 UT) on 8 September 2017, and h'F at Sanya station exhibited considerable increase simultaneously. This eastward IEF corresponds to eastward PPEF. In addition, the evolution of TEC depletion and ROTI fluctuation were also consistent with the variation of IMF B_z, IEF E_y, and SYM-H, which collectively show that it was the PPEF that drove the development of equatorial plasma bubbles.

Second, recent studies have shown that the PPEF can persist with considerably longer durations of ~8–10 hr if the IMF B_z is sustained southward for prolonged periods (Huang et al., 2005; Huang, 2008). Recall from Figure 1b that during the second main phase of the storm on 8 September, the IMF B_z suddenly dropped to −17.4 nT at 11:55 UT and remained southward for several hours, which suggests that there was a continuous PPEF since 12:00 UT. Moreover, some studies found that the PPEF could be eastward even at 22–23 LT (e.g., Chakrabarty et al., 2015; Fejer et al., 2008), which may be the case for this event that is evidenced in Figure 7, which shows that significant equatorial plasma depletions were measured along path #3 of Swarm A and path #8 of Swarm C at around 15.5 UT (~22 LT). It appears therefore that a possible extension of the upward vertical drift toward longer duration due to the consistent PPEF might have contributed to the bubble growth rate.

Third, one important aspect regarding the plots from Figures 2 to 5 is that the TEC irregularity traces were displaced westward in the successive plots and further the declination of the traces with the N-S meridian increases as time increases. These characteristics suggest that the irregularity structures drift westward with velocity increasing with increasing latitude. Since the observation of bubbles was preceded by the first main phase of storm event about 12 hr earlier, there is possibility of atmospheric gravity waves that generated in auroral zone and propagated equatorward, which could create TID that acted on the field-aligned bubble traces to shape such a latitude-dependent drift.

Last but not least, midlatitude plasma irregularities can either be an extension of depleted plasma bubbles from the equator (e.g., Cherniak & Zakharenkova, 2016; Huang et al., 2007; Katamzi-Joseph et al., 2017; Ma & Maruyama, 2006) or generated due to the atmospheric gravity waves and/or coupling between Perkins and sporadic E (E_s) layer instabilities, which will manifest in the form of TID (e.g., Li, Ning, Zhao, et al., 2009; Shiokawa et al., 2002, 2003; Tsugawa et al., 2007). Considering nighttime medium-scale TID could generate stream-like structures with southwestward propagation direction, it is very likely that both mechanisms played a role in current study. The storm time PPEF initiated the uplift of equatorial plasma bubbles and generated the latitudinal extension of the plasma depletions, while the TID might further facilitate the stretch of this structure and make it tilt more westward. Thus, the vertical drift velocity and the highest altitude of the equatorial plasma bubbles that estimated in the previous section are likely to be the upper limit. More work needs to be done in the future to distinguish the effects between plasma bubbles and TID.

5. Conclusion

This study presented unique observations of super plasma bubbles with bifurcated structures in the evening sector within China and adjacent areas (20°–45°N and 80°–110°E) during a storm on 8 September 2017. The existence and characteristics of the plasma bubbles were well indicated by the following results: (1) significant GNSS TEC decrease for 5–15 TECU and Swarm Ne depletions for 2–3 orders of magnitude, (2) enhancement of ionospheric h'F and associated equatorial plasma uplifts over certain stations after strongly southward turning of IMF, and (3) severe regional irregularities in ROTI map that is aligned with the TEC depletion structure. It has been shown that the plasma bubbles and uplifts were triggered by eastward PPEF. The upward drift speed of equatorial plasma bubbles was as much as 700 m/s at around 13 UT and gradually decreased with altitude and time. This study provides useful evidence in demonstrating the link between equatorial and midlatitude electrodynamics. The observed plasma depletions persisted for several hours and expanded northwestward along the magnetic field lines to midlatitude regions, which could be attributed to both equatorial plasma bubbles and medium-scale TID. The highest latitude where the depletions reached was around 50°N (MLAT: 45.5°N), which suggests that the plasma bubbles might reach an apex height of 6,600 km over the magnetic equator. However, this estimation is likely to be an upper limit since the transition of depletion signature from one of plasma bubbles to that of TID is not well defined, which need to be studied in the future.

Acknowledgments
This work is sponsored by the National Key R&D Program of China (2016YFB0501503), National Science Foundation of China (41404125 and 41674183), and Youth Innovation Promotion Association of Chinese Academy of Sciences. This research is also supported by AFOSR under DDDAS (Dynamic Data-Driven Applications Systems http://www.1dddas.org/) grant FA9550-16-1-0071. S. Zou acknowledges NASA NNX14AF31G and NSF AGS 1342968. The CMONOC data are available from the National Earthquake Infrastructure Service of China after registration approval via email at (cmonoc@seis.ac.cn). The IGS data are acquired from NASA Earth Science Data Systems that archived and distributed by the Crustal Dynamics Data Information System (CDDIS). The IMF B_z and IEF E_y data are obtained from the NASA Goddard Space Flight Center Omniweb Interface (https://omniweb.gsfc.nasa.gov). ASY-H and SYM-H indices are obtained from the World Data Center for Geomagnetism, Kyoto University (wdc.kugi.kyoto-u.ac.jp). We greatly appreciate the University of Massachusetts Lowell for providing ionosonde data from the DIDB database of Global Ionospheric Radio Observatory (https://spase.info/SMWG/Observatory/GIRO).

References

Aa, E., Huang, W., Liu, S., Shi, L., Gong, J., Chen, Y., & Shen, H. (2015). A regional ionospheric TEC mapping technique over China and adjacent areas: GNSS data processing and DINEOF analysis. *Science China Information Sciences*, *58*(10), 1–11. https://doi.org/10.1007/s11432-015-5399-2

Abadi, P., Otsuka, Y., & Tsugawa, T. (2015). Effects of pre-reversal enhancement of E *B* drift on the latitudinal extension of plasma bubble in Southeast Asia. *Earth Planets, and Space*, *67*, 74. https://doi.org/10.1186/s40623-015-0246-7

Abdu, M. A. (2012). Equatorial spread F/plasma bubble irregularities under storm time disturbance electric fields. *Journal of Atmospheric and Terrestrial Physics*, *75*, 44–56. https://doi.org/10.1016/j.jastp.2011.04.024

Abdu, M. A., Batista, I. S., Takahashi, H., MacDougall, J., Sobral, J. H., Medeiros, A. F., & Trivedi, N. B. (2003). Magnetospheric disturbance induced equatorial plasma bubble development and dynamics: A case study in Brazilian sector. *Journal of Geophysical Research*, *108*, 1449. https://doi.org/10.1029/2002JA009721

Abdu, M. A., Sastri, J. H., MacDougall, J., Batista, I. S., & Sobral, J. H. A. (1997). Equatorial disturbance dynamo electric field longitudinal structure and spread F: A case study from GUAR/EITS Campaigns. *Geophysical Research Letters*, *24*, 1707–1710. https://doi.org/10.1029/97GL01465

Basu, S., Basu, S., Groves, K. M., MacKenzie, E., Keskinen, M. J., & Rich, F. J. (2005). Near-simultaneous plasma structuring in the midlatitude and equatorial ionosphere during magnetic superstorms. *Geophysical Research Letters*, *32*, L12S05. https://doi.org/10.1029/2004GL021678

Basu, S., Basu, S., Groves, K. M., Yeh, H.-C., Su, S.-Y., Rich, F. J., et al. (2001). Response of the equatorial ionosphere in the South Atlantic Region to the Great Magnetic Storm of July 15, 2000. *Geophysical Research Letters*, *28*, 3577–3580. https://doi.org/10.1029/2001GL013259

Basu, S., Basu, S., Rich, F. J., Groves, K. M., MacKenzie, E., Coker, C., et al. (2007). Response of the equatorial ionosphere at dusk to penetration electric fields during intense magnetic storms. *Journal of Geophysical Research*, *112*, A08308. https://doi.org/10.1029/2006JA012192

Bhattacharyya, A., Basu, S., Groves, K. M., Valladares, C. E., & Sheehan, R. (2001). Dynamics of equatorial F region irregularities from spaced receiver scintillation observations. *Geophysical Research Letters*, *28*, 119–122. https://doi.org/10.1029/2000GL012288

Carter, B. A., Yizengaw, E., Pradipta, R., Retterer, J. M., Groves, K., Valladares, C., et al. (2016). Global equatorial plasma bubble occurrence during the 2015 St. Patrick's Day storm. *Journal of Geophysical Research: Space Physics*, *121*, 894–905. https://doi.org/10.1002/2015JA022194

Chakrabarty, D., Rout, D., Sekar, R., Narayanan, R., Reeves, G. D., Pant, T. K., et al. (2015). Three different types of electric field disturbances affecting equatorial ionosphere during a long-duration prompt penetration event. *Journal of Geophysical Research: Space Physics*, *120*, 4993–5008. https://doi.org/10.1002/2014JA020759

Cherniak, I., Krankowski, A., & Zakharenkova, I. (2014). Observation of the ionospheric irregularities over the Northern Hemisphere: Methodology and service. *Radio Science*, *49*, 653–662. https://doi.org/10.1002/2014RS005433

Cherniak, I., & Zakharenkova, I. (2016). First observations of super plasma bubbles in Europe. *Geophysical Research Letters*, *43*, 11,137–11,145. https://doi.org/10.1002/2016GL071421

Farley, D. T., Bonelli, E., Fejer, B. G., & Larsen, M. F. (1986). The prereversal enhancement of the zonal electric field in the equatorial ionosphere. *Journal of Geophysical Research*, *91*, 13,723–13,728. https://doi.org/10.1029/JA091iA12p13723

Fejer, B. G. (1991). Low latitude electrodynamic plasma drifts—A review. *Journal of Atmospheric and Terrestrial Physics*, *53*, 677–693. https://doi.org/10.1016/0021-9169(91)90121-M

Fejer, B. G., Jensen, J. W., & Su, S.-Y. (2008). Seasonal and longitudinal dependence of equatorial disturbance vertical plasma drifts. *Geophysical Research Letters*, *35*, L20106. https://doi.org/10.1029/2008GL035584

Fejer, B. G., Scherliess, L., & de Paula, E. R. (1999). Effects of the vertical plasma drift velocity on the generation and evolution of equatorial spread F. *Journal of Geophysical Research*, *104*, 19,859–19,870. https://doi.org/10.1029/1999JA900271

Foster, J. C., & Rich, F. J. (1998). Prompt midlatitude electric field effects during severe geomagnetic storms. *Journal of Geophysical Research*, *103*, 26,367–26,372. https://doi.org/10.1029/97JA03057

Horvath, I., & Lovell, B. C. (2013). Equatorial westward electrojet impacting equatorial ionization anomaly development during the 6 April 2000 superstorm. *Journal of Geophysical Research: Space Physics*, *118*, 7398–7409. https://doi.org/10.1002/2013JA019311

Huang, C.-S. (2008). Continuous penetration of the interplanetary electric field to the equatorial ionosphere over eight hours during intense geomagnetic storms. *Journal of Geophysical Research*, *113*, A11305. https://doi.org/10.1029/2008JA013588

Huang, C.-S., Foster, J. C., & Kelley, M. C. (2005). Long-duration penetration of the interplanetary electric field to the low-latitude ionosphere during the main phase of magnetic storms. *Journal of Geophysical Research*, *110*, A11309. https://doi.org/10.1029/2005JA011202

Huang, C.-S., Foster, J. C., & Sahai, Y. (2007). Significant depletions of the ionospheric plasma density at middle latitudes: A possible signature of equatorial spread F bubbles near the plasmapause. *Journal of Geophysical Research*, *112*, A05315. https://doi.org/10.1029/2007JA012307

Huang, C.-S., Rich, F. J., & Burke, W. J. (2010). Storm time electric fields in the equatorial ionosphere observed near the dusk meridian. *Journal of Geophysical Research*, *115*, A08313. https://doi.org/10.1029/2009JA015150

Katamzi-Joseph, Z. T., Habarulema, J. B., & Hernández-Pajares, M. (2017). Midlatitude postsunset plasma bubbles observed over europe during intense storms in April 2000 and 2001. *Space Weather*, *15*, 1177–1190. https://doi.org/10.1002/2017SW001674

Kelley, M. C., Haerendel, G., Kappler, H., Valenzuela, A., Balsley, B. B., Carter, D. A., et al. (1976). Evidence for a Rayleigh-Taylor type instability and upwelling of depleted density regions during equatorial spread F. *Geophysical Research Letters*, *3*, 448–450. https://doi.org/10.1029/GL003i008p00448

Kelley, M. C., Makela, J. J., Ledvina, B. M., & Kintner, P. M. (2002). Observations of equatorial spread-F from Haleakala, Hawaii. *Geophysical Research Letters*, *29*, 2003. https://doi.org/10.1029/2002GL015509

Kelley, M. C., Makela, J. J., Paxton, L. J., Kamalabadi, F., Comberiate, J. M., & Kil, H. (2003). The first coordinated ground- and space-based optical observations of equatorial plasma bubbles. *Geophysical Research Letters*, *30*, 1766. https://doi.org/10.1029/2003GL017301

Kil, H. (2015). The morphology of equatorial plasma bubbles—A review. *Journal of Astronomy and Space Sciences*, *32*, 13–19. https://doi.org/10.5140/JASS.2015.32.1.13

Kil, H., Paxton, L. J., Su, S.-Y., Zhang, Y., & Yeh, H. (2006). Characteristics of the storm-induced big bubbles (SIBBs). *Journal of Geophysical Research*, *111*, A10308. https://doi.org/10.1029/2006JA011743

Li, G., Ning, B., Liu, L., Wan, W., & Liu, J. Y. (2009). Effect of magnetic activity on plasma bubbles over equatorial and low-latitude regions in East Asia. *Annales de Geophysique*, *27*, 303–312. https://doi.org/10.5194/angeo-27-303-2009

Li, G., Ning, B., Zhao, B., Liu, L., Wan, W., Ding, F., et al. (2009). Characterizing the 10 November 2004 storm-time middle-latitude plasma bubble event in Southeast Asia using multi-instrument observations. *Journal of Geophysical Research*, *114*, A07304. https://doi.org/10.1029/2009JA014057

Ma, G., & Maruyama, T. (2006). A super bubble detected by dense GPS network at east Asian longitudes. *Geophysical Research Letters*, *33*, L21103. https://doi.org/10.1029/2006GL027512

Makela, J. J., & Kelley, M. C. (2003). Field-aligned 777.4-nm composite airglow images of equatorial plasma depletions. *Geophysical Research Letters*, *30*, 1442. https://doi.org/10.1029/2003GL017106

Mendillo, M., Hickey, D., Martinis, C., Wroten, J., & Baumgardner, J. (2018). Space weather nowcasting for area-denied locations: Testing all-sky imaging applications at geomagnetic conjugate points. *Space Weather*, *16*, 47–56. https://doi.org/10.1002/2017SW001741

Mendillo, M., Zesta, E., Shodhan, S., Sultan, P. J., Doe, R., Sahai, Y., & Baumgardner, J. (2005). Observations and modeling of the coupled latitude-altitude patterns of equatorial plasma depletions. *Journal of Geophysical Research*, *110*, A09303. https://doi.org/10.1029/2005JA011157

Ott, E. (1978). Theory of Rayleigh-Taylor bubbles in the equatorial ionosphere. *Journal of Geophysical Research*, *83*, 2066–2070. https://doi.org/10.1029/JA083iA05p02066

Perkins, F. (1973). Spread F and ionospheric currents. *Journal of Geophysical Research*, *78*, 218–226. https://doi.org/10.1029/JA078i001p00218

Pi, X., Mannucci, A. J., Lindqwister, U. J., & Ho, C. M. (1997). Monitoring of global ionospheric irregularities using the Worldwide GPS Network. *Geophysical Research Letters*, *24*, 2283–2286. https://doi.org/10.1029/97GL02273

Ramsingh, S., Sreekumar, S., Banola, S., Emperumal, K., Tiwari, P., & Kumar, B. S. (2015). Sripathi low-latitude ionosphere response to super geomagnetic storm of 17/18 March 2015: Results from a chain of ground-based observations over Indian sector. *Journal of Geophysical Research: Space Physics*, *120*, 10,864–10,882. https://doi.org/10.1002/2015JA021509

Retterer, J. M., & Roddy, P. (2014). Faith in a seed: On the origins of equatorial plasma bubbles. *Annales de Geophysique*, *32*, 485–498. https://doi.org/10.5194/angeo-32-485-2014

Scherliess, L., & Fejer, B. G. (1997). Storm time dependence of equatorial disturbance dynamo zonal electric fields. *Journal of Geophysical Research*, *102*, 24,037–24,046. https://doi.org/10.1029/97JA02165

Shiokawa, K., Otsuka, Y., Ogawa, T., Balan, N., Igarashi, K., Ridley, A. J., et al. (2002). A large-scale traveling ionospheric disturbance during the magnetic storm of 15 September 1999. *Journal of Geophysical Research*, *107*, 1088. https://doi.org/10.1029/2001JA000245

Shiokawa, K., Ihara, C., Otsuka, Y., & Ogawa, T. (2003). Statistical study of nighttime medium-scale traveling ionospheric disturbances using midlatitude airglow images. *Journal of Geophysical Research*, *108*(A1), 1052. https://doi.org/10.1029/2002JA009491

Tsugawa, T., Otsuka, Y., Coster, A. J., & Saito, A. (2007). Medium-scale traveling ionospheric disturbances detected with dense and wide TEC maps over North America. *Geophysical Research Letters*, *34*, L22101. https://doi.org/10.1029/2007GL031663

Tsunoda, R. T. (1980). Magnetic-field-aligned characteristics of plasma bubbles in the nighttime equatorial ionosphere. *Journal of Atmospheric and Terrestrial Physics*, *42*, 743–752. https://doi.org/10.1016/0021-9169(80) 90057-4

Tsunoda, R. T., Livingston, R. C., McClure, J. P., & Hanson, W. B. (1982). Equatorial plasma bubbles—Vertically elongated wedges from the bottomside F layer. *Journal of Geophysical Research*, *87*, 9171–9180. https://doi.org/10.1029/JA087iA11p09171

Tulasi Ram, S., Kumar, S., Su, S.-Y., Veenadhari, B., & Ravindran, S. (2015). The influence of Corotating Interaction Region (CIR) driven geomagnetic storms on the development of equatorial plasma bubbles (EPBs) over wide range of longitudes. *Advances in Space Research*, *55*, 535–544. https://doi.org/10.1016/j.asr.2014.10.013

Tulasi Ram, S., Rama Rao, P. V. S., Prasad, D. S. V. V. D., Niranjan, K., Gopi Krishna, S., Sridharan, R., & Ravindran, S. (2008). Local time dependent response of postsunset ESF during geomagnetic storms. *Journal of Geophysical Research*, *113*, A07310. https://doi.org/10.1029/2007JA012922

Woodman, R. F., & La Hoz, C. (1976). Radar observations of F region equatorial irregularities. *Journal of Geophysical Research*, *81*(31), 5447–5466. https://doi.org/10.1029/JA081i031p05447